Observation of stochastic resonance in directed propagation of cold atoms

Alexander Staron,[1,*] Kefeng Jiang,[1,*] Casey Scoggins,[1] Daniel Wingert,[1] David Cubero,[2] and Samir Bali[1,†]
[1]*Department of Physics, Miami University, Oxford, Ohio 45056-1866, USA*
[2]*Departamento de Fisica Aplicada I, Universidad de Sevilla, Sevilla, Spain*

(Received 4 September 2022; accepted 15 November 2022; published 26 December 2022)

Randomly diffusing atoms confined in a dissipative optical lattice are illuminated by a weak probe of light. The probe transmission spectrum reveals directed atomic propagation that occurs perpendicular to the direction of probe beam propagation. Resonant enhancement of this directed propagation is observed as we vary the random photon scattering rate. We experimentally characterize this stochastic resonance as a function of probe intensity and lattice well depth. A simple model reveals how the probe-excited atomic density waves and optical pumping rates conspire to create directed atomic propagation within a randomly diffusing sample.

DOI: 10.1103/PhysRevResearch.4.043211

Random fluctuations dominate the transport of submicroscopic systems immersed in a noisy environment, e.g., spontaneous emission recoils in the case of resonantly illuminated cold atoms. The ability of "Brownian ratchets" to convert random fluctuations into useful directed motion is a central topic in nonequilibrium statistical physics that was carefully explored in theory and experiment [1–3]. In particular, the phenomenon of "stochastic resonance," which refers to a peak in system response as a function of increasing noise strength, has received wide attention in the physics community [4–6], even finding application in climate science [7], biology [8], and, more recently, in engineering [9,10]. It was pointed out that naturally occurring protein motors are able to power the processes of life by harnessing energy from surrounding Brownian fluctuations with efficiencies that are orders of magnitude larger than any artificial nanomachine built to date [11]. Thus the notion that the controlled addition of random noise fluctuations may help rather than hinder system performance has important implications for optimizing the efficiency of nanodevices [12] and sensors [13,14] in situations where environmental noise is significant.

Cold atoms confined in dissipative optical potentials [15], where spontaneous emission is significant, are an ideal testbed to study stochastic resonance: The system (i.e., the confining potential) and the random environmental noise (i.e., spontaneous emission recoils, or thermal collisions) can be independently varied by adjusting beam parameters. Recently, in an experiment, stochastic resonances were detected in cold atoms in a dissipative double-well potential formed by splitting a magnetooptical trap with a blue-detuned sheet of light: Random thermal collisions caused the atoms to hop between the two wells and stochastic resonances were observed in the interwell hopping rate as a function of temperature, while also varying barrier height and atom number [16].

In this work, we report on the observation and experimental characterization of stochastic resonance in the directed propagation of cold atoms confined in a dissipative optical lattice. Here, the transfer between adjacent wells of the periodic potential array is caused by stochastic optical pumping processes. In previous work, stochastic resonance in a dissipative lattice was predicted [17,18], and preliminary evidence was observed by modulating the lattice potential and detecting a resonant enhancement in small center-of-mass displacements of the diffusing atom cloud [19]. In contrast, we reveal stochastic resonance via pump-probe spectroscopy, which permits a first experimental exploration of the dependence of the stochastic resonance on the lattice well depth and the strength of lattice modulation. A new theory [20], based on the decomposition of the current into its atomic density wave contributions, elucidates how probe-modulated ground-state potentials and optical pumping rates conspire to generate resonantly enhanced directed propagation.

We consider cold atoms in a so-called three-dimensional (3D)-lin⊥lin configuration [15,18], formed by confining the $F_g = 1/2 \leftrightarrow F_e = 3/2$ atoms in an optical lattice created by the superposition of four red-detuned laser beams of amplitude $\mathcal{E}_0$ and frequency ω_L. Two beams lie in the plane xOz, with angle θ_x, counterpropagating to the other two, which are in the plane yOz with angle θ_y, as illustrated in Fig. 1(a). The beams produce two light-shifted ground-state $\pm 1/2$-spin potentials $U_\pm(x, y, z)$ with well depth U_0 shown in Fig. 1(b) (see Appendices A and B). We focus on movement along the x-direction. A one-dimensional model arises after neglecting movement in the other perpendicular directions [17–19,21]. By formally considering $y = z = 0$, the optical potential in each ground state is given by [15,18]

$$U_\pm(x) = \frac{U_0}{4}[-3 - \cos(2k_x x) \pm 2\cos(k_x x)], \qquad (1)$$

[*]These authors contributed equally to this work.
[†]Corresponding author: balis@miamioh.edu

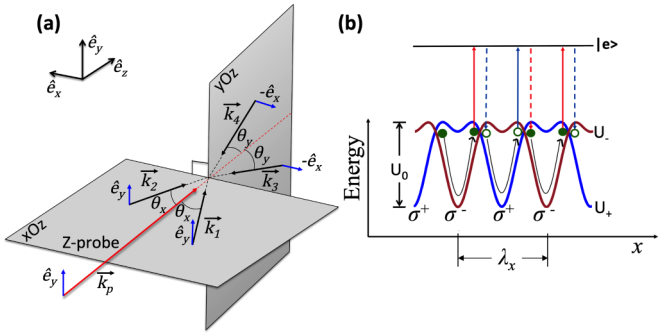

FIG. 1. (a) Scheme of the 3D tetrahedral lin⊥lin lattice. (b) Optical potential $U_\pm$ along the x-direction ($y = z = 0$) seen by a $F_g = 1/2 \rightarrow F_e = 3/2$ atom in the above lattice, with well-depth U_0 and spatial periodicity $\lambda_x = 2\pi/k_x$.

with transition probability rates between them given by

$$\gamma_\pm(x) = \frac{2\Gamma_S}{9}[3 + \cos(2k_x x) \pm 4\cos(k_x x)], \tag{2}$$

where $k_x = k_L \sin\theta_x$, k_L is the laser beam wave number, $U_0 = -16\hbar\Delta_0'/3$, Δ_0' (<0) is the light-shift per lattice field, and Γ_S is the photon scattering rate per lattice beam. We checked that, within the parameter range studied here, semiclassical simulations [22,23] of the 3D and one-dimensional (1D) systems provide qualitatively equivalent results. In each ground state, atoms oscillate in optical wells with vibrational frequency

$$\Omega_X = k_x\sqrt{\frac{3U_0}{2m}} = 4\sin\theta_x\sqrt{|\Delta_0'|\,\omega_r}, \tag{3}$$

where $\omega_r = \hbar k_L^2/(2m)$ is the recoil frequency. But this motion is not uninterrupted, the interaction with the laser also produces random absorption-emission processes with the excited states (collectively denoted by $|e\rangle$). Photon scattering is viewed as noise, analogous to Brownian fluctuations in thermal systems, occasionally pumping an atom into the other ground state sublevel at the rate $\gamma_\pm$ (2) and causing spatial diffusion [18,24]. The transitions are most likely at the peaks of the potential barriers, a distance π/k_x from the bottom of the well, yielding the well-known Sisyphus damping, where atoms mostly "climb hills," continuously dissipating energy.

Since the atoms are most likely pumped to a neighboring well via sublevel transitions at the turning points in their oscillations, after half a time period π/Ω_X, the average velocity associated with this half oscillation is given by $v_S = \Omega_X/k_x$. Once in the new ground-state sublevel, it takes another half a period π/Ω_X to reach the turning point on the other side of the well, also half a period length π/k_x away. However, with no symmetry breaking element at play, each step can proceed with equal probability to the right or the left, yielding zero current.

The introduction of a weak probe $\mathcal{E}_p$, ω_p propagating in the z-direction, as in Fig. 1(a), breaks the symmetry resulting in directed motion along $\pm x$: $\mathcal{E}_p$ modulates the lattice at $\delta = \omega_L - \omega_p$ producing the following addition to the optical potentials:

$$U_\pm^p(x,t) = -2U_0\varepsilon_p\cos k_x x\cos\delta t, \tag{4}$$

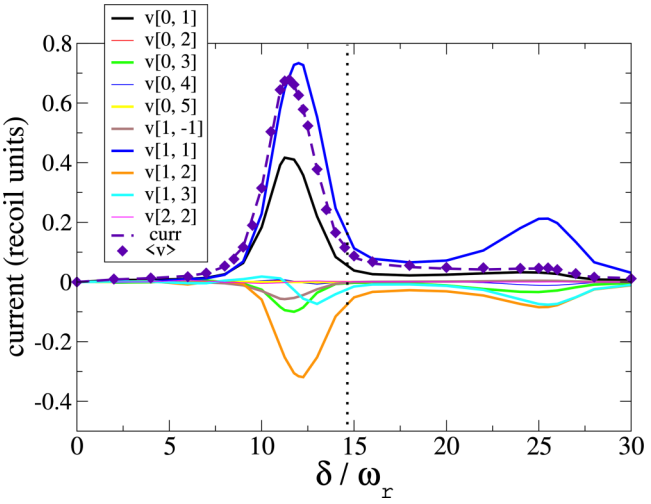

FIG. 2. Contribution to the current $v[l,n]$ of the atomic density wave with frequency $\omega = l\delta$ and wave number $k = nk_x$ under a probe-induced lattice modulation traveling in the $+x$-direction (6) with $\varepsilon_p = 0.1$, from a semiclassical simulation with $U_0 = 400\,\hbar\omega_r$ and $\Gamma_S = 5.7\,\omega_r$, $\theta_x = 25^0$. The dashed line is the sum of all contributions and the diamonds the current calculated directly in the simulation. The vertical dotted line indicates the vibrational frequency Ω_X.

where $\varepsilon_p = \mathcal{E}_p/4\mathcal{E}_0$. Since

$$\cos k_x x\cos\delta t = \tfrac{1}{2}[\cos(-k_x x - \delta t) + \cos(+k_x x - \delta t)], \tag{5}$$

the probe contribution (4) can be seen as the superposition of two perturbations traveling in opposite directions with velocity $\pm\delta/k_x$. Each perturbation is expected to excite an atomic density wave with wave number $k = \pm k_x$ and frequency $\omega = \delta$, referred to as Brillouin modes in analogy to acoustic waves rippling through fluids [17,21]. Optimal propagation is then expected when the velocity of these atomic modes, $v_B = \pm\delta/k_x$, matches that of the half-oscillations discussed above, v_S, yielding a maximum at $\delta = \Omega_X$. Previous research [17–19,21] focused only on these modes, which share the same frequency and wave number as the probe perturbations (a simple visualization is provided in Appendix C). The results of a novel theory [20], presented in Fig. 2, do confirm them as the dominant ones, though other excited density waves can be clearly observed at play with nonnegligible quantitative contributions.

In general, a propagating perturbation is expected to excite not only the atomic wave of frequency and wave number of the perturbation, but also other nearby modes. This is indeed the case in our system, Fig. 2 shows that atomic waves with $\omega = \delta$ and $k = 2k_x$ and $3k_x$ are also excited, as well as the mode $\omega = 2\delta$, $k = 2k_x$, which has the same phase velocity as the propagating perturbation, in addition to a plethora of nonpropagating modes (i.e., with $\omega = 0$).

However, mode excitation is not sufficient to guarantee a significant contribution to the directed motion. In Brownian ratchets [1–3], the quantity of interest is the current, defined as the average velocity $\langle v\rangle = \lim_{t\to\infty}[\langle x(t)\rangle - \langle x(0)\rangle]/t$. A novel theoretical development [20] was able to express analytically the current as an expansion $\langle v\rangle = \sum_{l,n} v[l,n]$,

where $v[l,n]$ is proportional to the Fourier amplitude of the atomic density wave with frequency $\omega = l\delta$ and wave number $k = nk_x$. The analytical calculation is based on the coupled Fokker-Planck equations resulting from the semiclassical approximation [23]. Figure 2 shows the results for the optical lattice (1) to (2) modulated by the $+x$-propagating part of the probe potential in (4) to (5)

$$U_{\pm}^{p}(x) = -U_0\varepsilon_p \cos(k_x x - \delta t). \tag{6}$$

The good agreement between the current obtained directly in the simulations (diamonds) and the sum of all the mode contributions (dashed line) serves as a validation of the analytical calculations [20].

As discussed above, optimal transport for atoms following the density mode $\omega = \delta, k = k_x$ is expected when its propagation is synchronized with the most likely transitions between the ground-state sublevels, the latter happening at half oscillations in the potential wells, and thus at $\delta \approx \Omega_X$. Here an atom could be hopping between states after half oscillations while riding at a maximum of the atomic wave. Indeed, the strongest peak observed in Fig. 2 takes place at a frequency slightly below Ω_X. The expression used for the vibrational frequency (3) is based on a harmonic approximation for small deviations about the well's bottoms, actually underestimating the time spent in the half oscillation, and thus, overestimating the optimal frequency.

A second peak, though of considerably smaller amplitude, can be seen at double this optimal frequency in Fig. 2, indicating a further synchronization mechanism between the two propagation processes. It can be also readily rationalized, as in these conditions, during a half oscillation time, the atomic wave, traveling at two times the previous speed, can still offer a density maximum at the same places where the atomic transitions are most likely, the potential barriers.

Note that Fig. 2 shows important contributions to the directed motion coming from other modes. In particular, the atomic wave with $\omega = \delta$, $k = 2k_x$ is observed to produce a current, slightly less than half the contribution of the probe's mode, in the opposite direction. In this case the atomic wave is moving with half the speed $\delta/(2k_x)$ and has half the wavelength $2\pi/(2k_x)$, thus there is an extra density maximum within the well length $2\pi/k_x$. Under these conditions, an atom moving in the direction of the probe-modulated potential (6) has higher speed than the wave and is less likely to cross a density maximum than when moving in the opposite direction, thus favoring that reversed direction.

Moreover, Fig. 2 shows that the contribution to the current from the mode with $\omega = 0$, $k = k_x$ is slightly more than half the contribution of the dominant mode, and is therefore relevant. This kind of nonpropagating mode is responsible for directed motion in rocking ratchets [1], where the driving force is usually chosen to be unbiased and nonpropagating. Here the mode, like all modes shown in Fig. 2, is also observed to be optimally excited at about the vibrational frequency, owing to the discussed matching of δ with the intrinsic frequency Ω_X.

Note that the transition rates $\gamma_{\pm}$ define another intrinsic frequency of the unperturbed lattice. Taking the spatial average of (2) results in $\gamma_0 = 2\Gamma_S/3$, the average number of atomic transitions per unit time.

Thus, a *resonant enhancement* of atoms undergoing directed propagation is expected when γ_0 is synchronized with δ and Ω_X. Specifically, the most coherent motion is expected when there is a single transition every half oscillation, $\gamma_0(\pi/\Omega_X) \approx 1$, yielding the prediction [18]

$$\Gamma_S \approx \frac{6}{\pi}\sin\theta_x\sqrt{|\Delta_0'|\omega_r}. \tag{7}$$

Optimization of the unidirectional propagation is therefore expected when the random photon scattering process Γ_S is tuned to the value given by (7). This is stochastic resonance [17–19], which we demonstrate experimentally via pump-probe spectroscopy below.

Our experiments are performed in a standard 3D tetrahedral lin⊥lin lattice, depicted in Fig. 1(a), comprising four equally intense near-resonant red-detuned beams ($1/e^2$-diameter, 9.2 mm; $\theta_x = \theta_y = 25°$) that confine about 10^8 ^{85}Rb atoms ($\sim$30 μK), i.e., only a few percent of the wells are occupied by an atom. We introduce a weak y-polarized z-propagating probe beam (Z-probe) of intensity I_p with $1/e^2$-diameter 1.4 mm ($\lesssim$ diameter of cold atom cloud) at frequency ω_p. The lattice beams collectively serve as the pump at fixed frequency ω. The probe frequency ω_p is scanned around ω and probe transmission is measured as a function of the pump-probe detuning δ. The intensity for a single lattice beam I ranges from 1.48 to 14.5 mW/cm^2 (total lattice intensity $= 4I$), and the lattice is red-detuned by $\Delta = 3.5 - 17\ \Gamma$ from the ^{85}Rb $F_g = 3 \rightarrow F_e = 4$ D_2 transition (natural linewidth $\Gamma/2\pi = 6.07$ MHz). In all cases $\delta/\omega < 10^{-9}$ and the intensity ratio of probe-to-single lattice beam is $|\mathcal{E}_p/\mathcal{E}_0|^2 < 4\%$, i.e., $I_p/4I < 1\%$, or $\epsilon_p < 0.05$.

To explore stochastic resonance we tune the random noise Γ_S without changing the optical lattice, described by well depth U_0. From (A1) to (A5), we see that if we tune lattice intensity I and detuning Δ such that the ratio I/Δ remains constant, we may vary Γ_S ($\propto I/\Delta^2$) without changing U_0 ($\propto I/\Delta$).

Figure 3(a) shows the probe transmission spectrum for a specific lattice well-depth. A spectral feature denoted Ω_Z arises because the Z-probe induces Raman transitions between adjacent vibrational levels in each well [21], in this case separated by $\sim \pm 170$ KHz. The peak (dip) corresponds to photons absorbed from a pump beam (the probe) and emitted into the probe (a pump beam). Further, we observe Brillouin resonances denoted as Ω_B which are a signature of directional transport as explained below. Figure 3(b) shows that the observed Ω_Z and Ω_B values, as the well depth is varied, are in good agreement with the calculated values, shown by lines, for Ω_Z (A5) and Ω_X (3), respectively.

The features Ω_B, despite coinciding with $\pm\Omega_X$, cannot arise from nonpropagating atoms oscillating inside wells because the Z-probe operator is quadratic in x (Appendix D). Instead, the Z-probe interferes with the lattice beams, producing propagating modulations that drive directed transport. Note that the contributions to the pump-probe spectrum from two of the four lattice beams $\vec{k}_3$ and $\vec{k}_4$ are suppressed due to Doppler broadening in the z-direction [25].

The interference of the $\hat{y}$-polarized probe with $\hat{y}$-polarized lattice beams $\vec{k}_1$, $\vec{k}_2$ ($|\vec{k}_{1,2}| = |\vec{k}_p| = k$) generates a propagating *intensity* modulation in directions $\pm x$ (4) and (5). As

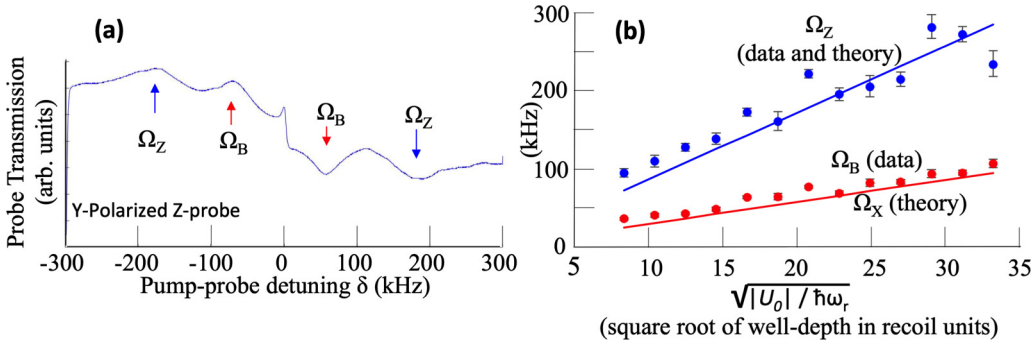

FIG. 3. (a) Typical probe transmission spectrum for the 3D tetrahedral lin⊥lin lattice with weak y-polarized z-propagating probe, at well depth $|U_0|/\hbar = 276\ \omega_r$ ($I = 5.2$ mW/cm^2, $\Delta = -12\Gamma$; 10 ms for each scan). We observe a feature Ω_Z at $\sim \pm 170$ kHz, and additional resonances Ω_B at $\sim \pm 60$ kHz which arise from probe-induced directed atomic transport along $\pm x$. (b) Measured values for Ω_Z and Ω_B versus well-depth agree with calculations (lines) of the z-component of the vibrational frequency and x-component Ω_X, respectively (see text). Here, ω_r is the ^{85}Rb recoil frequency 3.86 kHz. No fitting parameters are used.

discussed above, optimal directed propagation is expected at $\delta = \pm\Omega_X$, precisely the features marked Ω_B in Fig. 3(a). This velocity class, instead of diffusing in all directions, is ratcheted along $\pm x$, yielding a bidirectional ratchet.

In a significant departure from previous works, we shift attention from the location of the peak Ω_B to the *peak-amplitude* $\mathcal{A}$ which is proportional to the *number of atoms ratcheted* along $\pm x$. Figures 4 and 5 show measurements of $\mathcal{A}$ in the probe-modulated 3D lattice as a function of the stochastic noise rate Γ_S. Each data point is an average $\mathcal{A}$-value measured from at least five scans similar to Fig. 3(a) (see inset of Fig. 4), using a curve-fitting procedure (Appendix E). If the number of atoms initially confined in the lattice is kept the same (within 7% in our case), and I/Δ is held constant as we vary Γ_S, the $\mathcal{A}$-values are a measure of the directed atomic current for different noise rates.

Figure 4 shows clear evidence for stochastic resonance in a modulated cold atom optical lattice for three probe modulation strengths $I_p/4I$ ranging from 0.25% to 0.85%. Increasing the modulation strength results in larger atomic current, but since the lattice, and therefore vibrational frequency, remains unchanged we observe stochastic resonance at the same Γ_S-value. Atomic transport in this bidirectional ratchet falls off on either side of stochastic resonance, faster for low Γ_S-values since well-to-well transfer is disrupted more effectively if optical pumping simply does not occur. These observations concur with numerical simulations in [18] of the diffusion coefficient predicting enhanced transport along $\pm x$.

Furthermore, the noise rate at which stochastic resonance occurs is seen in Fig. 4 to be in very good agreement with the prediction of (7). This agreement is remarkable considering that the prediction uses a $F_g = 1/2 \rightarrow F_e = 3/2$ atom. In Fig. 5 we test the theory further by fixing the modulation strength and investigating stochastic resonance for several different well depths. In the inset we denote the noise rate at which stochastic resonance occurs as $(\Gamma_S)_{SR}$, and experimentally verify the linear dependence of $(\Gamma_S)_{SR}$ on the square root of the light shift Δ_0'. The requirement to keep the modulation strength fixed while varying well depth ($\propto I$) means that at the highest well depth the probe intensity is strong enough to perturb the lattice, while at the lowest well depth I_p is weak and barely excites Brillouin propagation, causing the data to depart from theory in both cases.

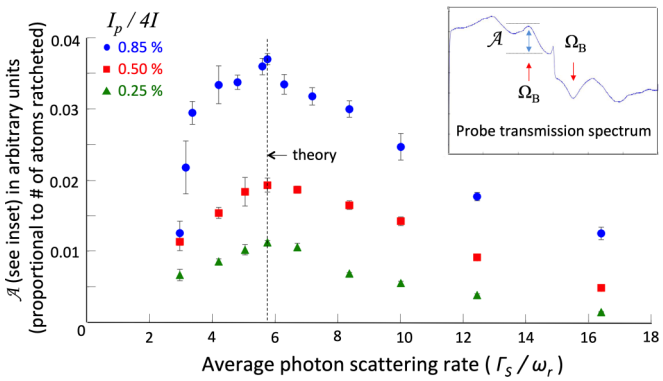

FIG. 4. Number of atoms ratcheted along $\pm x$ versus noise rate, or more specifically, amplitude of Brillouin peak Ω_B vs. Γ_S the photon scattering rate per lattice beam in units of recoil frequency ω_r, at a fixed well depth ($|U_0|/\hbar = 261\omega_r$). Stochastic resonance is observed at $\Gamma_S/\omega_r = 5.7$ irrespective of modulation amplitude, in agreement with theory (7).

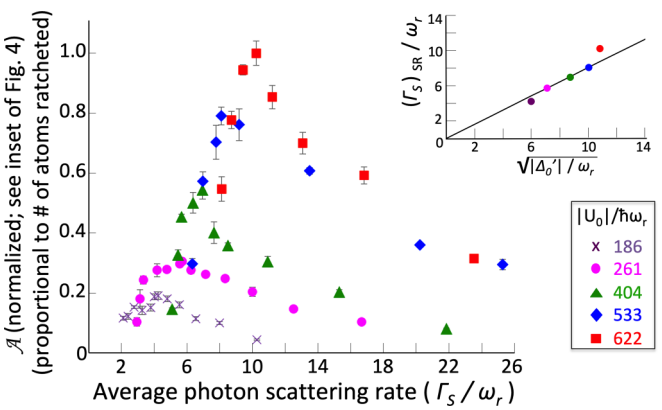

FIG. 5. Number of atoms ratcheted along $\pm x$ vs. noise rate for different well depths $|U_0|/\hbar\omega_r$ at fixed modulation strength $I_p/4I = 0.85\%$. Inset: The noise rate $(\Gamma_S)_{SR}$ at which stochastic resonance occurs scales linearly with $\sqrt{|\Delta_0'|}$, in good agreement with a theoretical line drawn using (7) with no fitting parameters.

In conclusion, we demonstrated stochastic resonance in a modulated dissipative optical lattice, as a function of the noise rate, the modulation amplitude, and the lattice well depth. By observing the transmission spectrum of a weak probe beam that modulates the lattice we present evidence that the photon scattering rate at which stochastic resonance occurs is independent of the modulation strength and that the stochastic resonance can be controlled by varying the lattice well depth. Remarkably, the data agree well with theory based on a simple $F_g = 1/2 \rightarrow F_e = 3/2$ atom without use of any fitting parameters. Furthermore, a recent novel theory permitted us to precisely determine the contribution to the directed motion of the atomic density waves excited by the perturbing probe and how they conspired with the optical pumping rates to create resonant directed propagation within a randomly diffusing cold atom cloud. We believe that this work may contribute toward the quest for artificial nanodevices that can operate in noisy environments with high efficiency [12–14]. A recent observation of stochastic resonance in quantum tunneling of an electron [26,27] reveals new directions where the source of the random noise is intrinsic quantum fluctuations in the system, instead of fluctuations in the environment.

This work is supported by the U.S. Army Research Laboratory and the U.S. Army Research Office under Grant Number W911NF2110120. DC acknowledges financial support from the Ministerio de Ciencia e Innovación of Spain, Grant No. PID2019-105316GB-I00. We thank the Instrumentation Laboratory at Miami University for electronics and LabView support. We thank A. Dharmasiri and A. Rapp for assistance during the initial setup. We are grateful to A. Reinhard and N. Peters for providing invaluable feedback on the manuscript.

APPENDIX A: 1D DISSIPATIVE OPTICAL LATTICE

Dissipative optical lattices are an ideal testbed for studying stochastic resonance because the stochastic coupling between the system (confined atom) and environment (random fluctuations in energy in the form of photon scattering) can be precisely controlled by varying the laser intensity and detuning, while ensuring that the lattice well depth remains constant. This essential point can be conveyed using well-known results for a 1D lin⊥lin lattice and a $F_g = 1/2 \rightarrow F_e = 3/2$ atom.

Two red-detuned laser beams of orthogonal linear polarization but same amplitude and wavelength λ, counterpropagate along the z-axis, yielding constant intensity but with steep polarization gradient of pitch $\lambda/2$. The two ground-state magnetic sublevels $m_{F_g} = \pm 1/2$ undergo polarization-dependent AC Stark shifts yielding spatially modulated potential wells which have maximum depth U_1 at sites of alternating pure circular polarization. Atoms settle at the bottoms of these wells. Their oscillatory excursions away from sites of pure circular polarization cause optical pumping to adjacent wells on either side, leading to diffusion along $\pm z$.

In the weak excitation limit, we obtain the following well-known expressions [15,18,28,29] for the light-shifted bipotential $U_{\pm}(z)$:

$$U_{\pm}(z) = \frac{U_1}{2}[-2 \pm \cos 2k_L z], \tag{A1}$$

the 1D lattice well depth U_1:

$$U_1 = -\frac{4}{3}\hbar\Delta_0{}' = -\frac{2}{3}\left(\frac{I/I_{\rm sat}}{1+4\Delta^2/\Gamma^2}\right)\hbar\Delta \propto \frac{I}{|\Delta|}, \tag{A2}$$

the intrawell vibrational frequency Ω_V:

$$\Omega_V = 2\sqrt{\omega_r U_1/\hbar} \propto \sqrt{\frac{I}{|\Delta|}}, \tag{A3}$$

and the position-dependent transition probability rates $\gamma_{\pm}$ between the ground-state potentials

$$\gamma_{\pm}(z) = \frac{2\Gamma_S}{9}(1 \pm \cos 2k_L z), \tag{A4}$$

where

$$\Gamma_S = \frac{\Gamma}{2}\left(\frac{I/I_{\rm sat}}{1+4\Delta^2/\Gamma^2}\right) \propto \frac{I}{\Delta^2}. \tag{A5}$$

Here I is the lattice laser intensity (per beam) and $I_{\rm sat}$ is the saturation intensity (1.67 mW/cm^2 for the ^{85}Rb D_2 $F_g = 3, m_{Fg} = \pm 3\rangle \rightarrow |F_e = 4, m_{Fe} = \pm 4\rangle$ $\sigma^{\pm}$ cycling transitions), Δ is the lattice laser detuning (<0), $\Gamma/2\pi$ is the natural linewidth and $\omega_r/2\pi$ is the recoil frequency (6.07 MHz and 3.86 kHz, respectively, for ^{85}Rb), $k_L = 2\pi/\lambda$, and z is the lattice axis. The relation $|\Delta| \gg \Gamma$ usually applies in practical situations. The ratio $(I/I_{\rm sat})/(1+4\Delta^2/\Gamma^2)$ is just the saturation parameter s_0 which is $\ll 1$ in the weak excitation limit. In our 3D lattice experiments s_0 ranges from about 0.001 to about 0.08. $\Delta_0{}' \equiv \Delta s_0/2$ is the light-shift per lattice beam for a closed transition having a Clebsch-Gordan coefficient equal to 1, in accordance with notation used in [15,18]. Finally, $\Gamma_S \equiv \Gamma s_0/2$ is the photon scattering rate per lattice beam [18].

From equations (A1) to (A5) we see that if we tune I and Δ such that I/Δ^2 varies but $I/|\Delta|$ stays constant, we can tune the stochastic noise given by the photon scattering rate Γ_S while keeping the lattice unchanged (because the well depth U_1 and vibrational frequency Ω_V stay constant). This ability to tune the stochastic noise while leaving the lattice unchanged makes the dissipative lattice a uniquely ideal testbed for investigating stochastic resonance.

APPENDIX B: 3D DISSIPATIVE TETRAHEDRAL OPTICAL LATTICE

Our experiments on stochastic resonance are carried out in a three-dimensional standard lin⊥lin dissipative "bright" optical lattice. A standard 3D tetrahedral lin⊥lin lattice consists of four overlapping equally intense near-resonant red-detuned beams as shown in Fig. 1(a). The total electric field now takes

the form [15]

$$\vec{E}(\vec{r},t) = \tfrac{1}{2}\mathcal{E}_0[e^{i\phi}\hat{e}_y(e^{i\vec{k}_1\cdot\vec{r}} + e^{i\vec{k}_2\cdot\vec{r}}) + \hat{e}_x(e^{i\vec{k}_3\cdot\vec{r}} + \hat{e}_x e^{i\vec{k}_4\cdot\vec{r}})]e^{-i\omega_L t} + \text{c.c.}$$

Here

$$\vec{k}_1\cdot\vec{r} = k_L(x\sin\theta_x + z\cos\theta_x),$$
$$\vec{k}_2\cdot\vec{r} = k_L(-x\sin\theta_x + z\cos\theta_x),$$
$$\vec{k}_3\cdot\vec{r} = k_L(x\sin\theta_y - z\cos\theta_y),$$
$$\vec{k}_4\cdot\vec{r} = k_L(-x\sin\theta_y - z\cos\theta_y),$$

where we make the choice $e^{i\phi} = -i$, as in [15].

For a $F_g = 1/2 \rightarrow F_e = 3/2$ atom confined in this 3D lattice the equations corresponding to (A1) to (A3) were derived in [15,18,29]

$$U_\pm(x,y,z) = \frac{U_0}{4}[-2 - \cos(2k_x x) - \cos(2k_y y) \pm 2\cos(k_x x)\cos(k_y y)\cos(k_z z)]. \quad \text{(B1)}$$

The $y = z = 0$ section of the potentials in (B1) is used in (1). Here, the 3D lattice well depth U_0 is given by

$$U_0 = -16\hbar\Delta_0'/3. \quad \text{(B2)}$$

The vibrational frequencies and position-dependent transition probability rates are given by

$$\Omega_{X,Y} = 4\sin\theta_{x,y}\sqrt{|\Delta_0'|\,\omega_r}, \quad \text{(B3)}$$

$$\Omega_Z = (\cos\theta_x + \cos\theta_y)\sqrt{|\Delta'|\,\omega_r}, \quad \text{(B4)}$$

$$\gamma_\pm(x,y,z) = \frac{2\Gamma_S}{9}[2 + \cos(2k_x x) + \cos(2k_y y) \pm 4\cos(k_x x)\cos(k_y y)\cos(k_z z)], \quad \text{(B5)}$$

where $k_x = k_L\sin\theta_x$, $k_y = k_L\sin\theta_y$, and $k_z = k_L(\cos\theta_x + \cos\theta_y)$. $\Omega_{X,Y,Z}$ are the x, y, z-components of the vibrational frequency Ω_V. Note that the expression for Ω_Z above is modified so as to be a better approximation for the case of a $F_g \geqslant 3 \rightarrow F_e = F_g + 1$ atom [15]. $\Delta' = 8\Delta_0{}'$ is the light shift at a point of circular polarization for a closed transition having a Clebsch-Gordan coefficient equal to 1. For the $F_g = 3 \rightarrow F_e = 4$ transition in ^{85}Rb, $I_{sat} = 1.64$ mW/cm^2 for σ-light.

In the experiments, a weak y-polarized probe beam of the form [15]

$$\vec{E}_p(z,t) = e^{i\phi}\,\hat{e}_y\,\mathcal{E}_p\,e^{i(k_p z - \omega_p t)} + \text{c.c.} \quad \text{(B6)}$$

propagating in the $+z$-direction ($\mathcal{E}_p \ll \mathcal{E}_0$) is made incident on the 3D lattice, as depicted in Fig. 1(a). This probe creates a lattice perturbation that propagates in the $\pm x$-directions, as discussed in the paper.

APPENDIX C: VISUALIZATION OF THE DOMINANT PROPAGATING MODE [1,1] IN FIG. 2

As discussed in the paper, a new theory [20] for Brillouin propagation in a 1D section of a 3D lattice decomposes the atomic current into the contributions from the different atomic density wave modes excited by the weak probe. For the dominant [1,1] mode the atomic density wave propagates at the same velocity as the propagating potential perturbation.

A depiction, as in Fig. 6, of the [1,1] mode offers instructive insights into how directed atomic propagation may arise within a sample of randomly diffusing atoms. The topmost

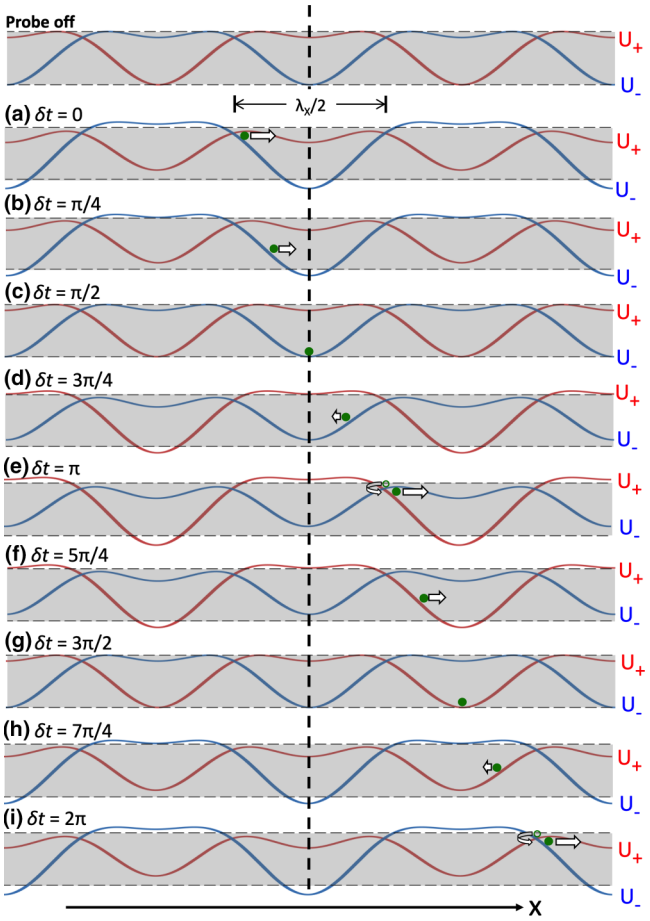

FIG. 6. Probe-modulated lattice potentials $U_\pm$, obtained by adding $U_\pm(x)$ and $U_\pm^p(x,t)$ in equations (1) and (4) of the main paper. Probe OFF: The well-depth of the unperturbed lattice bipotential is demarcated in all the plots by the dashed horizontal lines (shaded gray). The dashed vertical line indicates that the x-location for the wells stays fixed. (a)–(i) Probe ON: Snapshots of U_+ and U_- as they are modulated out-of-phase with each other. For the [1,1] mode, the time taken by an atom to complete one half-oscillation in the well equals the time taken to complete one half-modulation. For an atom starting at the top left of the U_- well at $\delta t = 0$ as shown, when the well is deepest, and moving with average velocity $+v_S = \Omega_X/k_x$, the atom experiences, on the average, a deeper well while rolling downhill, from (a) to (c), and a shallower well while rolling uphill, from (c) to (e). The white arrows depict the instantaneous force sensed by the atom. The net force forward during the half-cycle (a) to (e) balances the frictional force from Sisyphus cooling, enabling the atom to reach the top on the other side of the well, triggering an optical transition to the adjacent U_+ well which is at its deepest at that precise instant. Thus the motion repeats and the atom continues to propagate along $+x$ over many wells. The same directed propagation along $-x$ occurs for an atom starting at the top right of a U_- well at $\delta t = 0$ and moving with average velocity $-v_S$, leading to the creation of a bidirectional ratchet.

plot shows the unperturbed bipotential $U_{\pm}(x)$ from (1) when the probe is off. The gray region marks the sizes of the unperturbed well depths and the dashed vertical line marks the x-location of a particular well. The probe-modulated ground-state potentials, denoted in the figure by $U_{\pm}$, are simply obtained by adding the expressions for $U_{\pm}(x)$ in (1) and $U^{p}_{\pm}(x,t)$ in (4). We use $\epsilon_p = \mathcal{E}_p/4\mathcal{E}_0 = 0.1$, the same as in Fig. 2. This value of ϵ_p is more than twice the maximum value attained in our experiments and is used to exaggerate probe effects in Fig. 6 for visual clarity. As indicated in (5), the probe contributes two equal and opposite perturbations traveling in the $\pm x$-directions. The result is that the x-location of the wells stay fixed, but the depths of adjacent wells oscillate out-of-phase with each other. This is illustrated in Figs. 6(a) to 6(i), where successive snapshots of the probe-modulated potentials $U_{\pm}$ are plotted at $\delta t = 0, \pi/4, \pi/2$ and so on. Note that during the first half of the probe modulation cycle $\delta t = 0 \rightarrow \pi$ [Figs. 6(a) to 6(e)], U_{-} becomes shallower while U_{+} grows deeper, and the roles are reversed during the second half $\delta t = \pi \rightarrow 2\pi$ [Figs. 6(e) to 6(i)].

The vibrational frequency Ω_X coincides with the modulation frequency δ for the [1,1] mode. Atoms residing near the bottoms of wells are excited by this resonance, causing them to approach regions near the top of the wells where the probability for a transition to the adjacent well by optical pumping is larger. Consider an atom starting at the top of a U_{-} well, at $\delta t = 0$ when the well is deepest, on the left side as shown and moving with average velocity $+v_S = \Omega_X/k_x$. Because $\delta = \Omega_X$, the atom completes one half-oscillation in the well in the same time $\delta t = \pi$ that the modulation completes one half-cycle. A key point is that the well is on the average deeper while the atom is rolling downhill and shallower while rolling uphill. In Fig. 6, the white arrows depict the size and direction of the force at each instant on the atom (not the direction of motion of the atom; this atom is always moving to the right). This asymmetry results in a net force forward on the atom during its half-oscillation, which suppresses the effect of the ever-present frictional force due to Sisyphus cooling. The atom is thus able to reach the top of the well on the other side, triggering a transition to the adjacent well U_{+}, which at $\delta t = \pi$, happens to be at its deepest and the cycle repeats. The atom can undergo directed propagation in the $+x$-direction over many successive wells [17–19,21]. Of course, an atom starting at the top right of a U_{-} well, at $\delta t = 0$ when the well is deepest, and moving with average velocity $-v_S$, experiences exactly the same type of directed propagation over many wells in the $-x$-direction. Thus, we have a bidirectional ratchet.

APPENDIX D: Ω_B IN FIG. 3 COINCIDES WITH $\pm\Omega_X$ BUT IS EVIDENCE FOR DIRECTED PROPAGATION NOT INTRAWELL OSCILLATION

The z-propagating probe measures Ω_Z, but cannot measure Ω_X or Ω_Y. It is important to make this point because Ω_B happens to coincide with the calculated value for Ω_X. Figure 3(a) in the paper shows a Z-probe transmission spectrum for a specific lattice well depth. In order for a peak or a dip at a vibrational frequency component to arise in the probe transmission spectrum there must be a probe-induced Raman transition between adjacent intrawell quantized vibrational levels (say ϕ_n and ϕ_{n+1}, which have opposite parity). Since the probe $\vec{E}_p$ is weak, the dominant probe term in the total electric field is the lattice-probe interference term which goes as $\vec{E}_0 \cdot \vec{E}^{*}_p$ (see Appendix B). The Raman transition is proportional to the overlap integral $\int d\vec{r}\, \phi^{*}_{n+1} \vec{E}_0 \cdot \vec{E}^{*}_p \phi_n$. The product of the wave functions is always odd, therefore this integral is nonzero only if the interference term is odd. For the y-polarized Z-probe, the interference term goes as $\cos(k\, x \sin\theta_x) \exp[-ik\, z(1-\cos\theta_x)]$, which for small values of x and z is linear in z, but quadratic in x (we have taken $k_L = k_p = k$). Thus, the integrand of the overlap integral is even in z allowing for the detection of Raman transitions at Ω_Z in Fig. 3(a). However, the observed peak-dip features at Ω_X in Fig. 3(a) cannot arise from Raman transitions between adjacent vibrational levels because the integrand is an odd function in x. We explain in the paper that these spectral features arise from directional propagating modes along $\pm x$.

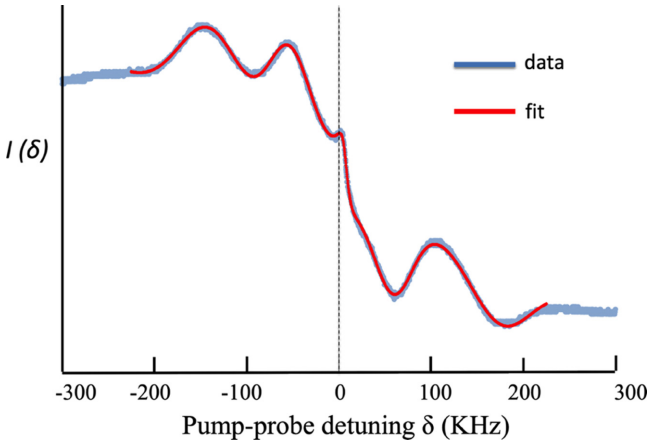

FIG. 7. The fit function $I(\delta)$ in (E1) is used to model the probe transmission spectrum.

APPENDIX E: CURVE-FITTING METHOD TO OBTAIN $\mathcal{A}$

The probe transmission spectrum in Fig. 3(a) is fit by a function $I(\delta)$, as shown in Fig. 7.

The fit function $I(\delta)$, given below, contains four Gaussian functions, two for the spectral peak and dip at the vibrational frequency $\pm\Omega_Z$ and two for the Brillouin peak/dip at $\pm\Omega_B$. $I(\delta)$ also contains Lorentzian and dispersive curves to help fit the central feature of the spectrum, referred to as the "Rayleigh" feature in the literature [15], believed to arise from atomic velocity damping due to Sisyphus cooling [30]. Finally, a linear and constant term are included to further improve the fitting

$$I(\delta) = A_{Z1} e^{-\frac{(\delta-\Omega_{Z1})^2}{2\sigma_{Z1}{}^2}} + A_{Z2} e^{-\frac{(\delta-\Omega_{Z2})^2}{2\sigma_{Z2}{}^2}} + A_{B1} e^{-\frac{(\delta-\Omega_{B1})^2}{2\sigma_{B1}{}^2}} + A_{B2} e^{-\frac{(\delta-\Omega_{B2})^2}{2\sigma_{B1}{}^2}} + a_1 + a_2\delta + \frac{a_3}{(\delta+x_0)^2+\gamma^2} + \frac{a_4(\delta+x_0)}{(\delta+x_0)^2+\gamma^2}. \quad \text{(E1)}$$

[1] D. Cubero and R. Renzoni, *Brownian Ratchets: From Statistical Physics to Bio and Nano-motors* (Cambridge University Press, Cambridge, England, 2016).

[2] P. Hänggi and F. Marchesoni, Artificial Brownian motors: Controlling transport on the nanoscale, Rev. Mod. Phys. **81**, 387 (2009).

[3] P. Reimann, Brownian motors: Noisy transport far from equilibrium, Phys. Rep. **361**, 57 (2002).

[4] T. Wellens, V. Shatokhin, and A. Buchleitner, Stochastic resonance, Rep. Prog. Phys. **67**, 45 (2004).

[5] L. Gammaitoni, P. Hänggi, P. Jung, and F. Marchesoni, Stochastic resonance, Rev. Mod. Phys. **70**, 223 (1998).

[6] K. Wiesenfeld and F. Moss, Stochastic resonance and the benefits of noise: from ice ages to crayfish and SQUIDs, Nature (London) **373**, 33 (1995).

[7] A. Ganopolski and S. Rahmstorf, Abrupt Glacial Climate Changes due to Stochastic Resonance, Phys. Rev. Lett. **88**, 038501 (2002).

[8] M. D. McDonnell and D. Abbott, What is stochastic resonance? Definitions, misconceptions, debates, and its relevance to biology, PLoS Comput. Bio. **5**, e1000348 (2009).

[9] B. Bhar, A. Khanna, A. Parihar, S. Datta, and A. Raychowdhury, Stochastic resonance in insulator-metal-transition systems, Sci. Rep. **10**, 5549 (2020).

[10] A. Dodda, A. Oberoi, A. Sebastian, T. Choudhury, J. Redwing, and S. Das, Stochastic resonance in MoS_2 photodetector, Nat. Commun. **11**, 4406 (2020).

[11] B. Lewandowski, G. De Bo, J. W. Ward, M. Papmeyer, S. Kuschel, M. J. Aldegunde, P. M. E. Gramlich, D. Heckmann, S. M. Goldup, D. M. D'Souza, A. E. Fernandes, and D. A. Leigh, Sequence-specific peptide synthesis by an artificial small molecule machine, Science **339**, 189 (2013).

[12] J. P. Pekola, Towards quantum thermodynamics in electronic circuits, Nat. Phys. **11**, 118 (2015).

[13] D. Mason, J. Chen, M. Rossi, Y. Tsaturyan, and A. Schliesser, Continuous force and displacement measurement below the standard quantum limit, Nat. Phys. **15**, 745 (2019).

[14] A. Heinrich, W. D. Oliver, L. M. K. Vandersypen, A. Ardavan, R. Sessoli, D. Loss, A. B. Jayich, J. Fernandez-Rossier, A. Laucht, and A. Morello, Quantum-coherent nanscience, Nat. Nanotechnol. **16**, 1318 (2021).

[15] G. Grynberg and C. Robilliard, Cold atoms in dissipative lattices, Phys. Rep. **355**, 335 (2001).

[16] I. Stroescu, D. Hume, and M. Oberthaler, Dissipative Double-Well Potential for Cold Atoms: Kramers Rate and Stochastic Resonance, Phys. Rev. Lett. **117**, 243005 (2016).

[17] L. Sanchez-Palencia, F. Carminati, M. Schiavoni, F. Renzoni, and G. Grynberg, Brillouin Propagation Modes in Optical Lattices: Interpretation in Terms of Nonconventional Stochastic Resonance, Phys. Rev. Lett. **88**, 133903 (2002).

[18] L. Sanchez-Palencia and G. Grynberg, Synchronization of Hamiltonian motion and dissipative effects in optical lattices: Evidence for a stochastic resonance, Phys. Rev. A **68**, 023404 (2003).

[19] M. Schiavoni, F. Carminati, L. Sanchez-Palencia, F. Renzoni, and G. Grynberg, Stochastic resonance in periodic potentials: Realization in a dissipative optical lattice, Europhys. Lett. **59**, 493 (2002).

[20] D. Cubero, arXiv:2208.08206.

[21] J.-Y. Courtois, S. Guibal, D. Meacher, P. Verkerk, and G. Grynberg, Propagating Elementary Excitation in a Dilute Optical Lattice, Phys. Rev. Lett. **77**, 40 (1996).

[22] P. Horak, J.-Y. Courtois, and G. Grynberg, Atom cooling and trapping by disorder, Phys. Rev. A **58**, 3953 (1998).

[23] K. Petsas, G. Grynberg, and J.-Y. Courtois, Semiclassical Monte Carlo approaches for realistic atoms in optical lattices, Eur. Phys. J. D **6**, 29 (1999).

[24] L. Sanchez-Palencia, P. Horak, and G. Grynberg, Spatial diffusion in a periodic optical lattice: Revisiting the Sisyphus effect, Eur. Phys. J. D **18**, 353 (2002).

[25] C. Jurczak, J.-Y. Courtois, B. Desruelle, C. I. Westbrook, and A. Aspect, Spontaneous light scattering from propagating density fluctuations in an optical lattice, Eur. Phys. J. D **1**, 53 (1998).

[26] T. Wagner, P. Talkner, J. Bayer, E. Rugeramigabo, P. Hänggi, and R. Haug, Quantum stochastic resonance in an a.c.-driven single-electron quantum dot, Nat. Phys. **15**, 330 (2019).

[27] S. Ludwig, Noise put to use, Nat. Phys. **15**, 310 (2019).

[28] J. Dalibard and C. Cohen-Tannoudji, Laser cooling below the Doppler limit by polarization gradients: simple theoretical models, J. Opt. Soc. Am. B **6**, 2023 (1989).

[29] K. I. Petsas, A. B. Coates, and G. Grynberg, Crystallography of optical lattices, Phys. Rev. A **50**, 5173 (1994).

[30] F.-R. Carminati, L. Sanchez-Palencia, M. Schiavoni, F. Renzoni, and G. Grynberg, Rayleigh Scattering and Atomic Dynamics in Dissipative Optical Lattices, Phys. Rev. Lett. **90**, 043901 (2003).